OPEN ACCESS

University of BRISTOL

Johns, M., Lewandowska, A., & Eichhorn, S. J. (2019). Rapid Determination of the Distribution of Cellulose Nanomaterial Aggregates in Composites Enabled by Multi-Channel Spectral Confocal Microscopy. *Microscopy and Microanalysis*, 25(3), 682-689. https://doi.org/10.1017/S1431927619000527

Peer reviewed version

Link to published version (if available):
10.1017/S1431927619000527

Link to publication record in Explore Bristol Research
PDF-document

University of Bristol - Explore Bristol Research

General rights

1   Rapid determination of the distribution of cellulose nanomaterial aggregates

2   in composites enabled by multi-channel spectral confocal microscopy

3

4   Marcus A. Johns, Anna E. Lewandowska, Stephen J. Eichhorn*

5   *Bristol Composites Institute (ACCIS), Department of Aerospace Engineering,*

6   *University of Bristol, Queens Building, University Walk, Bristol, BS8 1TR, UK*

7   Phone: +44 (0) 117 33 15650

8   E-mail: s.j.eichhorn@bristol.ac.uk

9

10   There is increased interest in the use of cellulose nanomaterials for the mechanical

11   reinforcement of composites due to their high stiffness and strength. However,

12   challenges remain in accurately determining their distribution within composite

13   microstructures. We report the use of a range of techniques used to image

14   aggregates of cellulose nanocrystals (CNCs) greater than 10 μm^2 within a model

15   thermoplastic polymer. Whilst Raman imaging accurately determines CNC

16   aggregate size, it requires extended periods of analysis and the limited observable

17   area results in poor reproducibility. In contrast, staining the CNCs with a

18   fluorophore enables rapid acquisition with high reproducibility, but overestimates

19   the aggregate size as CNC content increases. Multi-channel spectral confocal laser

20   scanning microscopy is presented as an alternative technique that combines the

21   accuracy of Raman with the speed and reproducibility of conventional confocal

22   laser scanning microscopy, enabling the rapid determination of CNC aggregate

23   distribution within composites.

24   *Keywords: cellulose, nanomaterials, composites, confocal microscopy, spectral*

25   *imaging, confocal Raman spectroscopy*

Introduction

26

27   The rise of the circular economy, and increased environmental awareness, has seen

28   biomaterials come to the fore of innovation as evidenced by the Circular Design

29   Challenge winners announced at the World Economic Forum Annual Meeting in

30   Davos in early 2018. These factors have led to significant interest in the use of

31   cellulosic nanomaterials (CNMs) across a wide range of application areas

32   including, but not exclusive to, composites (Nakagaito & Yano 2004, Malainine *et*

33   *al.* 2005), biosensors (Bi *et al.* 2016), drug delivery (Jackson *et al.* 2011), food

34   additives (Hu *et al.* 2016), packaging (Yu *et al.* 2014), energy storage (Liew *et al.*

35   2013), tissue engineering (He *et al.* 2014), and wastewater treatment (Batmaz *et al.*

36   2014). Their nanoscale dimensions, high mechanical properties, ease of

37   functionalization, and sustainability in particular have resulted in publications

38   exploring their use as reinforcement in various polymer nanocomposite materials

39   (Siró & Plackett 2010, Oksman *et al.* 2016, Kargarzadeh *et al.* 2017).

40   It is generally accepted that the uniform distribution of CNMs as a percolated

41   network throughout the polymer matrix results in composites with better

42   mechanical properties than those with isolated CNM aggregates. (Siqueira *et al.*

43   2010, Oksman *et al.* 2016, Ray & Sain 2016, Kargarzadeh *et al*. 2017, Chakrabarty

44   & Teramoto 2018) However, it is a particular challenge to track the bulk distribution

45   of CNMs in a nanocomposite material. Whilst electron microscopy can distinguish

46   individual CNMs (Ranby 1951), CNMs and polymeric materials have similar

47   densities, making contrast difficult without staining. Cellulose is also susceptible to

48   charge build-up and degradation under high energy beams (Foster *et al.* 2018,

49   Ogawa & Putaux 2018). Scanning probe microscopy has previously been used to

50   investigate the distribution of CNMs in composites (Saxena *et al*. 2009, Shariki *et*

51 *al*. 2011, Mandal & Chakrabarty 2015). Yet it is challenging to accurately

52 distinguish the CNMs from the polymer matrix via height mapping only – although

53 Nigmatullin *et al*. had success in distinguishing cellulose nanocrystals, CNCs, from

54 starch using adhesion mapping (Nigmatullin *et al*. 2018) – and the observable

55 volume is limited to around $150 \times 150 \times 15$ μm^3. Chemical mapping using confocal

56 Raman spectroscopy is a well-established technique (Stewart *et al*. 2012) that has

57 been successfully applied by Agarwal *et al*. to distinguish between CNCs and

58 polypropylene, mapping the density of CNCs in areas up to 100×100 μm^2

59 (Agarwal *et al*. 2012), whilst Lewandowska *et al*. have mapped areas containing

60 CNCs and polyethylene up to 200×200 μm^2 (Lewandowska & Eichhorn 2016,

61 Lewandowska *et al*. 2018). However, the observable area is still limited, and the

62 process time consuming, often requiring more than half a day to acquire and analyse

63 each image.

64 One alternative to these imaging approaches is the modification of CNMs with

65 various fluorophores, including fluorescein, rhodamine and calcofluor white

66 (Haghpanah *et al*. 2013, Lou *et al*. 2014, Endes *et al*. 2015, Camarero-Espinosa *et*

67 *al*. 2016, Tomić *et al*. 2016, Leng *et al*. 2017), which enables rapid imaging of their

68 bulk distribution in composites via confocal microscopy. However, the

69 physicochemical properties of the CNMs will inevitably be altered upon binding of

70 the fluorophore (Abitbol *et al*. 2013). Therefore, if the CNMs are modified with the

71 fluorophore before composite production, observations may not be representative

72 of the unmodified material.

73 It is generally accepted that fluorescent detection of CNMs requires the presence of

74 fluorophores due to the lack of fluorescent aromatic groups within their chemical

75 structure. Nevertheless, several publications have reported the autofluorescence of

3

76 cellulose under UV excitation (Olmstead & Gray 1993, Pöhlker *et al.* 2012, Gong

77 *et al.* 2013, Kalita *et al.* 2015, Malinowska *et al.* 2015, Johns *et al.* 2018). This

78 autofluorescence has previously been attributed to the presence of lignin in the

79 samples (Kalita *et al.* 2015). This effect is thought to be understood (Albinsson *et*

80 *al.* 1999, Radotić *et al.* 2006), but explanations for these materials do not hold true

81 for autofluorescent celluloses that are not of plant origin (Olmstead & Gray 1993,

82 Johns *et al.* 2018). Gong *et al.* suggest that the clustering of electron-rich groups

83 with lone pair electrons, *i.e.* oxygen atoms, resulting in electron cloud overlap are

84 responsible for the luminescent properties of carbohydrate molecules (Gong *et al.*

85 2013). The inter- and intra-molecular hydrogen bonding network between the

86 chains rigidify the molecular confirmations, blocking vibrational dissipation and

87 ensuring emission (Gong *et al.* 2013). This forms the basis of a theory known as

88 clustering-triggered emission (CTE) with computational modelling confirming that

89 interconnected short oxygen-oxygen contacts may exist between D-glucose units

90 (Yuan & Zhang 2017).

91 The present paper investigates the use of multi-channel spectral confocal laser

92 scanning microscopy, which simultaneously detects fluorescent emission across the

93 visible spectrum as 32 distinct channels rather than the single channel detected by

94 conventional confocal laser scanning microscopy, to track the distribution of CNMs

95 in a model HDPE composite material. The distribution of the CNM aggregates

96 observed using this technique is compared to those observed using confocal laser

97 scanning microscopy with conventional staining of the cellulose and confocal

98 Raman spectroscopy. It is reported that staining results in an overestimation of the

99 aggregate sizes, whilst limited analysis may be performed using data generated by

100 Raman spectroscopy due to the restricted observable area. Conversely, scanning

101   confocal microscopy enables the rapid analysis of the aggregate distribution whilst

102   maintaining the accuracy of Raman spectroscopy.

103   **Materials and Methods**

104   **Materials**

105   Freeze-dried cellulose nanocrystals (CNCs) were purchased from the University of

106   Maine, Process Development Centre; high density polyethylene (Arboblend HDPE;

107   molecular weight = 1.33×10^5 g mol^{-1}and melt volume flow rate = 2 cm^3 min^{-1})

108   was supplied by Tecnaro GmbH, while maleated polyethylene (A-C 575A, MAPE

109   copolymer) was provided by Honeywell. Calcofluor white stain was purchased

110   from Sigma Aldrich.

111   **Composite Sample Production**

112   The CNC/MAPE/HDPE composite samples were compounded with CNC loadings

113   of 0.625, 1.250, 2.500 and 5.000 wt.%. A procedure of compounding and extrusion

114   was consistent with a process previously described by Lewandowska and Eichhorn

115   (Lewandowska & Eichhorn 2016). Freeze-dried CNCs were used as purchased. All

116   compounds; filler, compatibilizer and matrix; were mixed in a mortar for 8 min and

117   subsequently were dried in a vacuum oven at a temperature of 60 °C for 24 h. The

118   compounding process was carried out in a counter rotating twin-screw extruder

119   (HAAKE Rheomex CTW5, Thermo Fisher Scientific) at a temperature of 160 °C

120   for 7 min at a speed of 70 rpm. The extruded filaments (ø ~ 2 mm) were cryo-

121   microtomed into slices of 20 µm thickness for further characterisation

122   (Lewandowska & Eichhorn 2016).

123

Scanning Electron Microscopy (SEM)

The morphology of the composites cross-sections was examined with a Nova 600 Dual Beam Scanning Electron Microscope (SEM) (FEI, Hillsboro, OR) with EDT detector. The SEM was operated at an acceleration voltage of 10 kV and a working distance of 5 mm. The composite sample was fixed on metal stubs using carbon tape and sputter-coated with a thin layer of palladium. The magnification used for the collection of SEM images was 100×.

Confocal Raman Spectroscopy (CRS)

Raman images were performed using a confocal Raman microscope (Alpha300, WITec GmbH). The spectrometer was equipped with a UHTS 300 VIS-NIR spectrograph optimized for NIR excitation and a thermoelectrically cooled CCD detector (down to -61 °C). Raman images were acquired using 785 nm wavelength laser (NIR) and 41 mW laser power at the sample for excitation of the Raman scattering. The sample was focused with a 50× objective lens (numerical aperture: 0.7, vertical resolution: 1.6 μm) with a lateral resolution of 684 nm. Each Raman image was recorded from an area of 200×200 μm^2 (40,000 μm^2) with a step size of 2 μm in both the *x*- and *y*- directions, using an exposure time of 4 s. Three images per composite sample were used in the analysis.

WITec Project Plus and Image J software were used to analyse Raman images. First, Raman images were converted into chemical images using cluster component analysis with WITec Project Plus. The estimation of the area of the CNC aggregates was conducted using Image J software. The extraction of the objects' dimensions was performed using an automated threshold with the algorithm 'IsoData'.

148 **Conventional Confocal Laser Scanning Microscopy (CCM)**

149 Samples were immersed in 0.3 mL calcofluor white stain for one minute before

150 removal and washing with DI water to remove excess dye. Samples were placed

151 between a glass slide and coverslip to flatten the surface. Z-stack images were

152 generated using a Zeiss LSM 880 confocal microscope (405 nm diode laser, 0.2 %

153 power, Plan-Apochromat 10x/0.45 M27 objective, MBS-405 filter, single channel

154 $\lambda = 410\text{-}523$ nm). The maximum distance between slices was 2 µm. Three replicates

155 were imaged per composite sample.

156 **Multi-Channel Spectral Confocal Laser Scanning Microscopy (SCM)**

157 Samples were placed between a glass slide and coverslip to flatten the surface.

158 Spectral z-stack images were generated using a Zeiss LSM 880 confocal

159 microscope (405 nm diode laser, 5.0 % power, Plan-Apochromat 10x/0.45 M27

160 objective, MBS-405 filter, 32 channels: $\lambda = 411\text{-}695$ nm). The maximum distance

161 between slices was 2 µm. Three replicates were imaged per composite sample.

162 **Image Processing**

163 Image stacks generated using conventional confocal microscopy and spectral

164 confocal microscopy were processed in Fiji. Briefly, the z-projection function

165 (projection type: standard deviation) was used to flatten image stacks into single

166 images. After thresholding (automatic values used for stained images; manual

167 adjustment of lower threshold value between 85-100 for spectral images), images

168 were analysed to determine the observed aggregate areas. Aggregates at the edge

169 of the images were excluded.

170

171

172   **Aggregate Distribution Analysis**

173   Aggregate distribution was subdivided into four categories: small, medium, large

174   and outliers. Rather than set these categories between fixed area values, which

175   could result in values being classified as outliers in box and whisker plots despite

176   being between two size categories, the maximum and minimum values were

177   determined using the box plots themselves. Briefly, a box plot was constructed

178   using the entire data set, and the values at which data would be classified as an

179   upper, or lower, outlier determined. The box plot was then regenerated using the

180   outlier values as the maximum and minimum for the data range and new outlier

181   values calculated. This process was repeated until the range of values fell between

182   the upper and lower outlier values. This determined the aggregates that fell into the

183   small category for each sample. To determine the medium category range, the

184   process was repeated excluding all values in the small category. The process was

185   finally repeated excluding values in the small and medium categories to define the

186   large category range. All values that fell out of these ranges, representing less than

187   2 % of aggregates observed in all samples, were classified as outliers. Due to the

188   skew present in the data sets, the calculated lower outlier values were always less

189   than the initial lower data values for all samples.

190   **Statistical Analysis**

191   Statistical analysis was performed using IBM SPSS Statistics software. For inter-

192   technique, pairwise comparison of the median CNC aggregate area, an independent

193   samples t-test was performed to determine the statistical difference between the

194   median values. For intra-technique comparison of the median CNC aggregate area,

195   intra-category CNC aggregate population analysis, and intra-category median

196   aggregate area, a one-way analysis of variance (ANOVA) test was used to

197 determine the statistical differences between two or more samples, assuming equal

198 variance, with Bonferroni posthoc correction. The Kruskal−Wallis one-way

199 ANOVA test was used to determine significant differences between the distribution

200 of values in each aggregate size category. In all cases, a confidence interval of 0.95

201 was used.

202 **Results and Discussion**

203 **Comparison of Multi-Channel Spectral Confocal Laser Scanning Microscopy**

204 **to Conventional Techniques**

205 Images of CNC aggregates embedded in a MAPE matrix at varying CNC contents

206 (0.625, 1.250, 2.500, and 5.000 wt.%) were obtained using conventional confocal

207 laser scanning microscopy, CCM, with cellulose stained using calcofluor white, and

208 with multi-channel spectral confocal laser scanning microscopy, SCM (Figures 1C

209 and D respectively). These were then compared to aggregates observed using SEM

210 and confocal Raman spectroscopy, CRS, mapping, previously reported by

211 Lewandowska *et al.* (Figures 1A and B).

212 Whilst there is apparent surface disruption in the SEM images, it is not possible to

213 confirm conclusively whether this is cellulose, and it is challenging to determine

214 the area of the aggregates. As such, this technique is not deemed suitable for further

215 analysis. CRS distinguishes between cellulose and the matrix by mapping the

216 intensity of wavenumbers attributable to cellulose and polyethylene at 1096 and

217 1295 cm^{-1} respectively. Comparison of the two enables chemical mapping of the

218 CNC aggregates (Supplementary Information Figure S1C). Whilst this method

219 accurately differentiates between the two materials, the observable area is limited

220 compared to the other techniques presented, which restricts the number of

221   observable aggregates (Table 1). CCM of the composite, where cellulose has been

222   stained with calcofluor white, enables an area 18 times greater than that viewable

223   with CRS to be observed. This enables the observation of more aggregates, whilst

224   theoretically maintaining the minimum observable aggregate size (Table 1). SCM

225   uses the same magnification as CCM, and, like the former technique, the relative

226   increase in the number of CNC aggregates observed compared to those observed

227   by CRS is equal to the relative increase in area (see Table 1). Despite there being

228   no stain, the CNC aggregates are readily distinguishable from the polymer matrix

229   due to differences in intensity and peak maxima (Figure 2) and can be matched to

230   aggregates identified using CCM (Supplementary Information, Figure S2). The

231   aggregates of CNCs exhibit fluorescence roughly an order of magnitude more

232   intense than the matrix, and have a peak maximum located in the range $\lambda = 464\text{-}473$

233   nm, whilst the matrix peak is located between $\lambda = 419\text{-}428$ nm. SCM also confirms

234   that CNCs are dispersed throughout the matrix, not just confined to the observed

235   aggregates, as evidenced by comparison of the matrix spectrum (Figure 2) to that

236   of the pure polymer (Supplementary Information, Figure S3). The matrix spectrum

237   clearly consists of both the polymer and CNC spectra, and can be discerned at a

238   glance. The presence of this dispersed material is more difficult to establish using

239   the other techniques – Raman requires deconvolution of the two spectra from one

240   another and a weak CNC signal may not be detected (Agarwal *et al*. 2012,

241   Lewandowska & Eichhorn 2016, Lewandowska *et al*. 2018). However, background

242   noise from the polymer – which risks the generation of false-positive results –

243   makes it difficult to confidently identify aggregates that are less than 11 μm^2 in

244   area, equivalent to 10 pixels, with the objective used. This limits the lower viewable

245   aggregate size compared to the other two techniques reported.

246   At each CNC wt.%, no significant difference between the mean CNC aggregate

247   areas, determined between 10 and 2,000 μm^2 due to the varying technique

248   resolution, is observed between the three techniques (Figure 3A). The exception

249   being the difference between the values calculated using SCM and CCM at a CNC

250   content of 5 wt.%. However, CRS and SCM are more closely aligned to one another

251   than CCM; the average significance between the calculated aggregate sizes for CRS

252   and SCM is 0.80 ± 0.07, compared to 0.27 ± 0.09 and 0.42 ± 0.19 between CRS

253   and CCM, and SCM and CCM respectively. As CNC content increases, a larger

254   number of aggregates may be analysed per sample (Table 1), which results in the

255   calculation of experimental mean values that are closer to the theoretically true

256   mean value. Therefore, it would be expected that significance between techniques

257   would increase as the CNC content increases as both techniques should be tending

258   towards the same mean value. Whilst this is observed between CRS and SCM,

259   indicating that the calculated values are more closely aligned as expected, the

260   significances between CRS and CCM, and SCM and CCM, both exhibit a negative

261   trend (Figure 3B). These results, taken with the calculated aggregate areas (Table

262   1.), indicate that CCM is overestimating the true mean aggregate value compared

263   to CRS and SCM, and that this overestimation increases as the CNC content

264   increases.

265   The use of CRS results in the greatest intra-sample error, due to the limited number

266   of aggregates observed, whilst staining of the cellulose results in the least intra-

267   sample variation. As a result of this, no significant difference is observed between

268   the mean CNC aggregate areas at varying CNC content for CRS, whilst the CCM

269   mean areas for 2.5 and 5 wt.% are both significantly different from each other, and

270   those for 0.625 and 1.25 wt.% (Figure 3A). SCM is somewhere between the two,

271   with the mean area for 5 wt.% being significantly different from that for 0.625 wt.%,

272 but neither being significantly different to the areas reported for 1.25 and 2.5 wt.%.

273 This indicates that the use of lower magnification for both confocal microscopy

274 techniques (CCM and SCM), resulting in a larger observable area and increase in

275 the number of aggregates analysed, improves reproducibility. This enables

276 significant differences to be observed between samples that are not observed for

277 CRS. However, the overestimation of the aggregate size using CCM may lead to

278 false significant differences being determined.

279 **CNC Aggregate Distribution as Determined by SCM and CCM**

280 The CNC aggregate area distribution within the polymer matrix is heavily skewed

281 towards smaller areas at all concentrations (Supplementary Information, Figure S4),

282 which is expected given that individual CNCs are only a few hundred nanometres

283 in length (Foster *et al*. 2018). A single box and whisker plot per sample was found

284 to be inappropriate for representing the data as outlying/anomalous results are

285 defined as being any value greater than the third quartile plus 1.5 times the

286 interquartile range, or lower than the first quartile minus 1.5 times the interquartile

287 range. This results in aggregates greater than $500\,\mu m^2$ being classified as anomalous

288 using conventional analysis, despite consistently being present in the samples

289 analysed. Therefore, an alternative approach to the analysis – detailed in the

290 methods section – was developed that split the aggregate distribution into small,

291 medium, large, and outlier categories, enabling different aggregate size ranges to

292 be analysed independently (Figure 4 and Table 2). CRS was not considered in this

293 analysis due to the limited number of aggregates that could be analysed (Table 1),

294 and aggregates $< 10\,\mu m^2$ were discarded for CCM to enable a direct comparison of

295 the two techniques.

296   For both techniques, a CNC content of 0.625 wt.% consistently results in the lowest

297   median and narrowest aggregate range across the three categories, whilst a CNC

298   content of 5 wt.% results in the largest median and aggregate range (Table 2).

299   However, SCM analysis reveals a similar trend to CRS as CNC content increases,

300   whereby the CNC content of 1.25 wt.% results in larger aggregate sizes than those

301   observed at 2.5 wt.%, whilst CCM analysis results in an increase in aggregate area

302   as the CNC content increases. Larger category ranges, resulting in larger median

303   aggregate sizes, are also observed for CCM. Population analysis of the categories,

304   whereby the sum of the categories is equal to 100 %, reveals no intra-category

305   significant difference across the CNC content range for SCM. However, a

306   significant decrease for aggregates that fall into the small category, from 76 to 61 %,

307   is observed as the CNC content increases for CCM. Likewise, a significant increase

308   for aggregates that fall into the large category, from 4 to 9 %, is also observed.

309   These data suggest that the presence of the stain, in conjunction with the analysis

310   method, results in aggregate size overestimation due to merging of multiple

311   individual aggregates, which consequently affects the population distribution. The

312   use of SCM removes this factor, improving the reliability of the determined

313   aggregate distribution.

314   **Conclusions**

315   Taking the statistical analysis for both inter- and intra-techniques into account,

316   evidence suggests that staining of CNCs results in an overestimation of the mean

317   aggregate area, which is exacerbated as the CNC content increases. Therefore,

318   despite providing highly reproducible results, CCM may not provide an accurate

319   representation of the distribution of CNC aggregates within a polymer matrix, as

320   demonstrated in the aggregate distribution analysis. This could lead to the reporting

321 of false significant differences between samples. In comparison, CRS may be the

322 most accurate technique for calculating the exact area of a CNC aggregate due to

323 the chemical mapping technique used. However, the limited number of observable

324 aggregates results in mean values that have a low reproducibility factor and

325 distribution analysis cannot be performed.

326 Here, SCM is presented as a novel technique for analysing CNC aggregates that

327 combines the reproducibility of CCM with the accuracy of CRS. This enables

328 precise observations on CNC aggregate distribution to be made with confidence.

329 The technique also demonstrates that, whilst CNCs aggregate together, CNCs are

330 distributed throughout the composite at a scale below that of the equipment

331 resolution, as evidenced by the presence of the cellulose spectra when analysing the

332 polymer background. This presents further opportunities for tracking CNC mixing

333 within composites.

344   **References**

345   Abitbol, T., Palermo, A., Moran-Mirabal, J.M. & Cranston, E.D. (2013).
346   Fluorescent Labeling and Characterization of Cellulose Nanocrystals with
347   Varying Charge Contents. *Biomacromolecules* **14**, 3278-3284.
348   Agarwal, U.P., Sabo, R., Reiner, R.S., Clemons, C.M. & Rudie, A.W. (2012).
349   Spatially Resolved Characterization of Cellulose Nanocrystal–Polypropylene
350   Composite by Confocal Raman Microscopy. *Appl. Spectrosc.* **66**, 750-756.
351   Albinsson, B., Li, S., Lundquist, K. & Stomberg, R. (1999). The origin of lignin
352   fluorescence. *J. Mol. Struct.* **508**, 19-27.
353   Batmaz, R., Mohammed, N., Zaman, M., Minhas, G., Berry, R.M. & Tam, K.C.
354   (2014). Cellulose nanocrystals as promising adsorbents for the removal of cationic
355   dyes. *Cellulose* **21**, 1655-1665.
356   Bi, Q., Dong, S., Sun, Y., Lu, X. & Zhao, L. (2016). An electrochemical sensor
357   based on cellulose nanocrystal for the enantioselective discrimination of chiral
358   amino acids. *Anal. Biochem.* **508**, 50-57.
359   Camarero-Espinosa, S., Rothen-Rutishauser, B., Weder, C. & Foster, E.J. (2016).
360   Directed cell growth in multi-zonal scaffolds for cartilage tissue engineering.
361   *Biomaterials* **74**, 42-52.
362   Chakrabarty, A. & Teramoto, Y. (2018). Recent Advances in Nanocellulose
363   Composites with Polymers: A Guide for Choosing Partners and How to
364   Incorporate Them. *Polymers* **10**, 517-563.
365   Endes, C., Mueller, S., Kinnear, C., Vanhecke, D., Foster, E.J., Petri-Fink, A.,
366   Weder, C., Clift, M.J.D. & Rothen-Rutishauser, B. (2015). Fate of Cellulose
367   Nanocrystal Aerosols Deposited on the Lung Cell Surface In Vitro.
368   *Biomacromolecules* **16**, 1267-1275.
369   Foster, E.J., Moon, R.J., Agarwal, U.P., Bortner, M.J., Bras, J., Camarero-
370   Espinosa, S., Chan, K.J., Clift, M.J.D., Cranston, E.D., Eichhorn, S.J., Fox, D.M.,
371   Hamad, W.Y., Heux, L., Jean, B., Korey, M., Nieh, W., Ong, K.J., Reid, M.S.,
372   Renneckar, S., Roberts, R., Shatkin, J.A., Simonsen, J., Stinson-Bagby, K.,
373   Wanasekara, N. & Youngblood, J. (2018). Current characterization methods for
374   cellulose nanomaterials. *Chem. Soc. Rev.* **47**, 2609-2679.
375   Gong, Y.Y., Tan, Y.Q., Mei, J., Zhang, Y.R., Yuan, W.Z., Zhang, Y.M., Sun, J.Z.
376   & Tang, B.Z. (2013). Room temperature phosphorescence from natural products:
377   Crystallization matters. *Sci. China: Chem.* **56**, 1178-1182.
378   Haghpanah, J.S., Tu, R., Da Silva, S., Yan, D., Mueller, S., Weder, C., Foster,
379   E.J., Sacui, I., Gilman, J.W. & Montclare, J.K. (2013). Bionanocomposites:
380   Differential Effects of Cellulose Nanocrystals on Protein Diblock Copolymers.
381   *Biomacromolecules* **14**, 4360-4367.
382   He, X., Xiao, Q., Lu, C., Wang, Y., Zhang, X., Zhao, J., Zhang, W., Zhang, X. &
383   Deng, Y. (2014). Uniaxially Aligned Electrospun All-Cellulose Nanocomposite
384   Nanofibers Reinforced with Cellulose Nanocrystals: Scaffold for Tissue
385   Engineering. *Biomacromolecules* **15**, 618-627.
386   Hu, Z., Marway, H.S., Kasem, H., Pelton, R. & Cranston, E.D. (2016). Dried and
387   Redispersible Cellulose Nanocrystal Pickering Emulsions. *ACS Macro Lett.* **5**,
388   185-189.
389   Jackson, J.K., Letchford, K., Wasserman, B.Z., Ye, L., Hamad, W.Y. & Burt,
390   H.M. (2011). The use of nanocrystalline cellulose for the binding and controlled
391   release of drugs. *Int. J. Nanomed.* **6**, 321-330.
392   Johns, M.A., Bae, Y., Guimarães, F.E.G., Lanzoni, E.M., Costa, C.A.R., Murray,
393   P.M., Deneke, C., Galembeck, F., Scott, J.L. & Sharma, R.I. (2018). Predicting

Ligand-Free Cell Attachment on Next-Generation Cellulose–Chitosan Hydrogels. *ACS Omega* **3**, 937-945.

Kalita, E., Nath, B.K., Agan, F., More, V. & Deb, P. (2015). Isolation and characterization of crystalline, autofluorescent, cellulose nanocrystals from saw dust wastes. *Ind. Crops Prod.* **65**, 550-555.

Kargarzadeh, H., Mariano, M., Huang, J., Lin, N., Ahmad, I., Dufresne, A. & Thomas, S. (2017). Recent developments on nanocellulose reinforced polymer nanocomposites: A review. *Polymer* **132**, 368-393.

Leng, T., Jakubek, Z.J., Mazloumi, M., Leung, A.C.W. & Johnston, L.J. (2017). Ensemble and Single Particle Fluorescence Characterization of Dye-Labeled Cellulose Nanocrystals. *Langmuir* **33**, 8002-8011.

Lewandowska, A.E. & Eichhorn, S.J. (2016). Quantification of the degree of mixing of cellulose nanocrystals in thermoplastics using Raman spectroscopy. *J. Raman Spectrosc.* **47**, 1337-1342.

Lewandowska, A.E., Inai, N.H., Ghita, O.R. & Eichhorn, S.J. (2018). Quantitative analysis of the distribution and mixing of cellulose nanocrystals in thermoplastic composites using Raman chemical imaging. *RSC Adv.* **8**, 35831-35839.

Liew, S.Y., Walsh, D.A. & Thielemans, W. (2013). High total-electrode and mass-specific capacitance cellulose nanocrystal-polypyrrole nanocomposites for supercapacitors. *RSC Adv.* **3**, 9158-9162.

Lou, Y.-R., Kanninen, L., Kuisma, T., Niklander, J., Noon, L.A., Burks, D., Urtti, A. & Yliperttula, M. (2014). The Use of Nanofibrillar Cellulose Hydrogel As a Flexible Three-Dimensional Model to Culture Human Pluripotent Stem Cells. *Stem Cells Dev.* **23**, 380-392.

Malainine, M.E., Mahrouz, M. & Dufresne, A. (2005). Thermoplastic nanocomposites based on cellulose microfibrils from Opuntia ficus-indica parenchyma cell. *Compos. Sci. Technol.* **65**, 1520-1526.

Malinowska, K.H., Rind, T., Verdorfer, T., Gaub, H.E. & Nash, M.A. (2015). Quantifying Synergy, Thermostability, and Targeting of Cellulolytic Enzymes and Cellulosomes with Polymerization-Based Amplification. *Anal. Chem.* **87**, 7133-7140.

Mandal, A. & Chakrabarty, D. (2015). Characterization of nanocellulose reinforced semi-interpenetrating polymer network of poly(vinyl alcohol) & polyacrylamide composite films. *Carbohydr. Polym.* **134**, 240-250.

Nakagaito, A.N. & Yano, H. (2004). The effect of morphological changes from pulp fiber towards nano-scale fibrillated cellulose on the mechanical properties of high-strength plant fiber based composites. *Appl. Phys. A* **78**, 547-552.

Nigmatullin, R., Harniman, R., Gabrielli, V., Muñoz-García, J.C., Khimyak, Y.Z., Angulo, J. & Eichhorn, S.J. (2018). Mechanically Robust Gels Formed from Hydrophobized Cellulose Nanocrystals. *ACS Appl. Mater. Interfaces* **10**, 19318-19322.

Ogawa, Y. & Putaux, J.-L. (2018). Transmission electron microscopy of cellulose. Part 2: technical and practical aspects. *Cellulose*.

Oksman, K., Aitomäki, Y., Mathew, A.P., Siqueira, G., Zhou, Q., Butylina, S., Tanpichai, S., Zhou, X. & Hooshmand, S. (2016). Review of the recent developments in cellulose nanocomposite processing. *Composites Part A* **83**, 2-18.

Olmstead, J.A. & Gray, D.G. (1993). Fluorescence emission from mechanical pulp sheets. *J. Photochem. Photobiol., A* **73**, 59-65.

443   Pöhlker, C., Huffman, J.A. & Pöschl, U. (2012). Autofluorescence of atmospheric
444   bioaerosols – fluorescent biomolecules and potential interferences. *Atmos. Meas.*
445   *Tech.* **5**, 37-71.
446   Radotić, K., Kalauzi, A., Djikanović, D., Jeremić, M., Leblanc, R.M. & Cerović,
447   Z.G. (2006). Component analysis of the fluorescence spectra of a lignin model
448   compound. *J. Photochem. Photobiol., B* **83**, 1-10.
449   Ranby, B.G. (1951). Fibrous macromolecular systems. Cellulose and muscle. The
450   colloidal properties of cellulose micelles. *Discuss. Faraday Soc.* **11**, 158-164.
451   Ray, D. & Sain, S. (2016). In situ processing of cellulose nanocomposites.
452   *Composites Part A* **83**, 19-37.
453   Saxena, A., Elder, T.J., Pan, S. & Ragauskas, A.J. (2009). Novel nanocellulosic
454   xylan composite film. *Composites Part B* **40**, 727-730.
455   Shariki, S., Liew, S.Y., Thielemans, W., Walsh, D.A., Cummings, C.Y., Rassaei,
456   L., Wasbrough, M.J., Edler, K.J., Bonné, M.J. & Marken, F. (2011). Tuning
457   percolation speed in layer-by-layer assembled polyaniline–nanocellulose
458   composite films. *J. Solid State Electrochem*. **15**, 2675-2681.
459   Siqueira, G., Bras, J. & Dufresne, A. (2010). Cellulosic Bionanocomposites: A
460   Review of Preparation, Properties and Applications. *Polymers* **2**, 728-765.
461   Siró, I. & Plackett, D. (2010). Microfibrillated cellulose and new nanocomposite
462   materials: a review. *Cellulose* **17**, 459-494.
463   Stewart, S., Priore, R.J., Nelson, M.P. & Treado, P.J. (2012). Raman Imaging.
464   *Annu. Rev. Anal. Chem*. **5**, 337-360.
465   Tomić, S., Kokol, V., Mihajlović, D., Mirčić, A. & Čolić, M. (2016). Native
466   cellulose nanofibrills induce immune tolerance in vitro by acting on dendritic
467   cells. *Sci. Rep.* **6**, 31618.
468   Yu, H., Yan, C. & Yao, J. (2014). Fully biodegradable food packaging materials
469   based on functionalized cellulose nanocrystals/poly(3-hydroxybutyrate-co-3-
470   hydroxyvalerate) nanocomposites. *RSC Adv.* **4**, 59792-59802.
471   Yuan, W.Z. & Zhang, Y. (2017). Nonconventional macromolecular luminogens
472   with aggregation-induced emission characteristics. *J. Polym. Sci. A* **55**, 560-574.

Table Legends

474   **Table 1**. Comparison of confocal techniques (confocal raman spectroscopy - CRS,

475   multi-channel spectral confocal laser scanning microscopy - SCM, and

476   conventional confocal laser scanning microscopy - CCM), highlighting differences

477   in aggregate size and number of aggregates observed. Error $\pm$ SE.

478   **Table 2.** Statistical analysis of data presented in Figures 4A and 4B. Analysis of

479   the range compares the distribution of values for each sample category irrespective

480   of the absolute values themselves. † $p < 0.05$ compared to 1.25 wt.% for a given

481   measurement; ‡ $p < 0.05$ compared to 2.5 wt.% for a given measurement; * $p < 0.05$

482   compared to 5 wt.% CNC for a given measurement.

483   **Figure Legends**

484   **Figure 1.** Representative images used to compare 5 wt.% CNC-MAPE composite

485   samples imaged using A) SEM (accelerating voltage: 10 kV, working distance: 5

486   mm, image acquisition: back scatter); B) Confocal Raman spectroscopy, CRS,

487   mapping at 1096 cm^{-1} (laser wavelength: 785 nm, laser power: 41 mW, lateral

488   resolution: 684 nm); C) Conventional confocal laser scanning microscopy, CCM,

489   (stain: calcofluor white, argon laser intensity: 0.2 %, single channel, λ = 410-523

490   nm); and D) Multi-channel spectral confocal laser scanning microscopy, SCM,

491   (argon laser intensity: 5.0 %, 32 channels, λ = 411-695 nm).

492   **Figure 2.** Comparison of typical spectra for CNC aggregates and a MAPE matrix.

493   Top: Spectra for CNC aggregates (bright bars, dashed line) and MAPE matrix (dark

494   bars, solid line) based on emission intensity. The CNC aggregates are more intense

495   than the background matrix, making it straightforward to distinguish between the

496   two. Bottom: Normalised spectra for CNC aggregates (dashed line) and MAPE

497   matrix (solid line). The peak range maxima for CNCs and MAPE are different, 464-

498   473 and 419-428 nm respectively, confirming that the two materials are

499   distinguishable. N = 3, n = 5.

500   **Figure 3.** A) Comparison of mean CNC aggregate areas as observed using CRS

501   (blue bars); SCM (red bars with rising diagonal lines); and CCM with CNCs stained

502   by calcofluor white (green bars with falling diagonal lines) at various CNC

503   contents. Alphanumeric labels signify intra-technique samples with no significant

504   difference between them. Due to the varying resolution of the three techniques,

505   values were calculated from aggregates between 10 and 2,000 μm^2, which are the

506   upper and lower ranges viewable for all three. * $p < 0.05$. N = 3, n $\geq$ 5. Error ± SE.

507   B) Change in significance between CRS and SCM (red squares); CRS and CCM

508   (blue circles); and SCM and CCM (green triangles) with increasing CNC content.

509   Logarithmic lines of best fit plotted to guide the eye.

510   **Figure 4.** Comparison of CNC aggregates at varying CNC content observed by

511   SCM and CCM. A, B: Box plots comparing distribution of aggregates between

512   samples obtained via A) SCM and B) CCM. Aggregates are divided into four

513   categories: small (blue boxes), medium (red boxes with light spot scattering), large

514   (green boxes with medium spot scattering), and outliers (black diamonds). The

515   mean values for each category are represented by open squares. Aggregates < 10

516   μm^2 ignored for analysis. $n > 425$. C, D: Populations for varying CNC content

517   obtained via C) SCM and D) CCM. Whilst no significant difference is observed

518   between each of the samples for SCM, differences are observed for CCM.

519   Aggregate categories: small (blue bars), medium (red bars with light spot

520   scattering), large (green bars with medium spot scattering), and outliers (yellow

521   bars with heavy spot scattering). For all categories $N = 3$. * $p < 0.05$ compared to 5

522   wt.% in the respective category. Error $\pm$ SE.

523
524
525
526
527
528
529
530
531
532
533
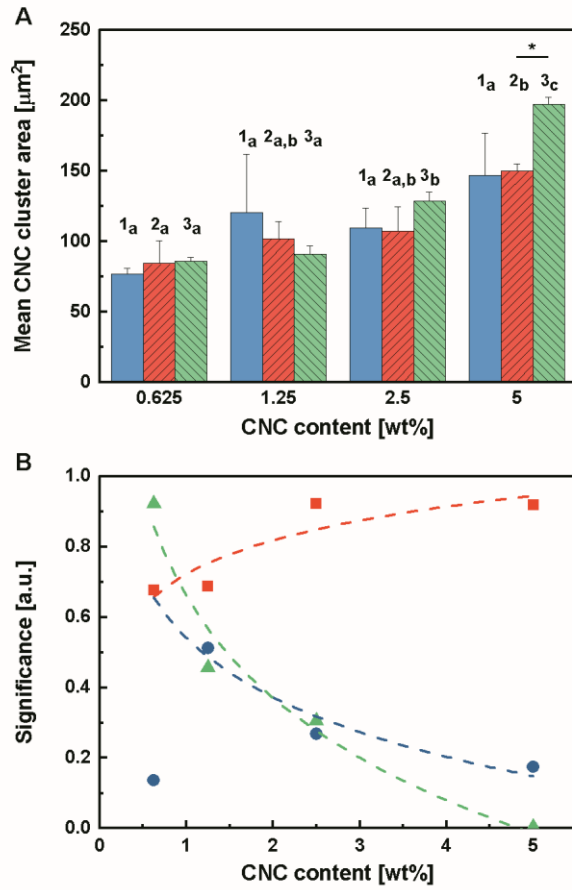534
535
536
537
538
539
540
541
542
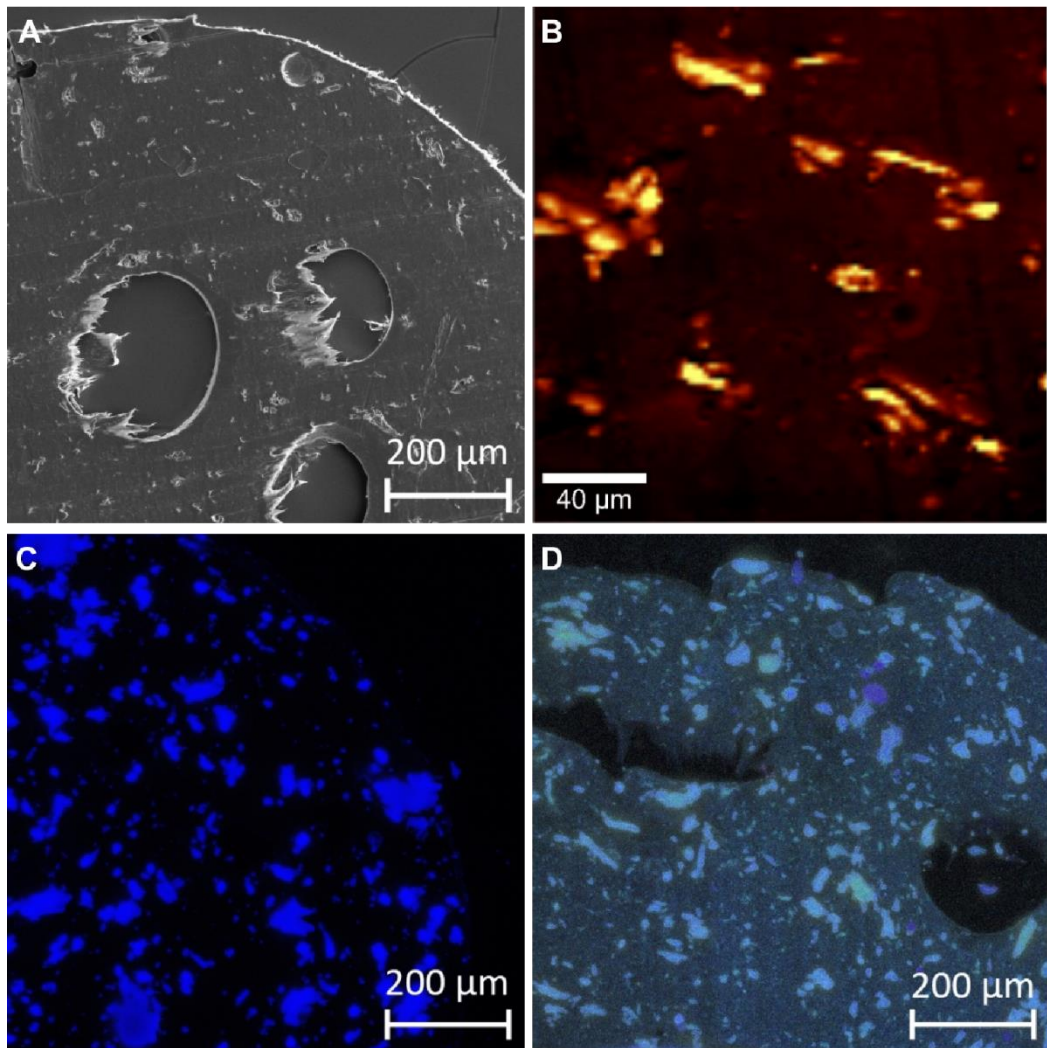
543
544
545 Figure 1
546
547
548
549
550
551
552
553
554
555
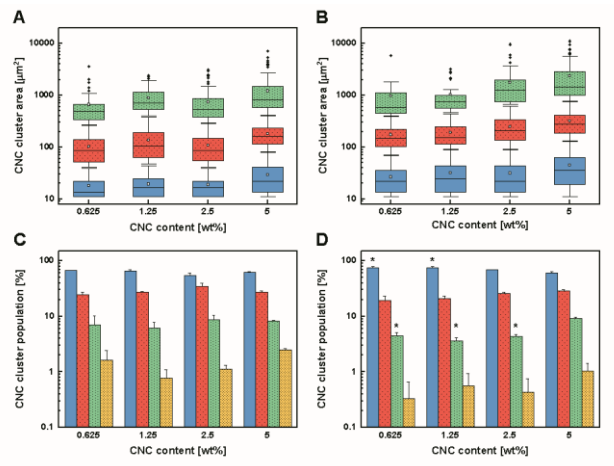556
557
558
559
560
561
562
563
564
565
566
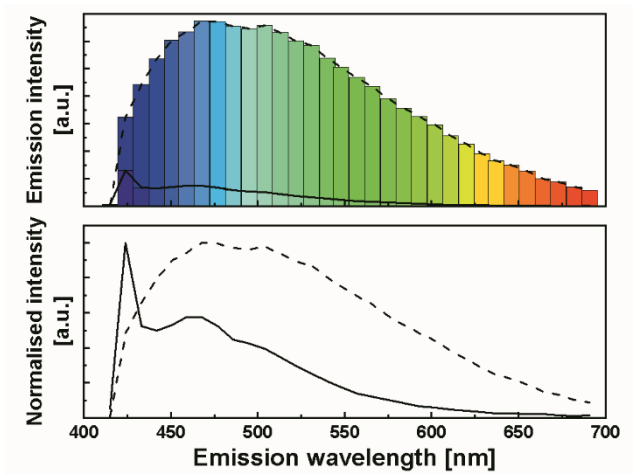
567
568
569   Figure 2
570
571
572
573
574
575
576
577
578
579
580
581
582
583
584
585
586
587
588
589
590
591
592
593
594
595
596
597
598
599
600
601
602
603
604
605
606

607
608 Figure 3
609
610
611
612
613
614
615
616
617
618
619
620
621
622
623
624
625
626
627
628
629
630
631
632
633

634
635
636 Figure 4
637
638
639
640
641
642
643
644
645
646
647
648
649
650
651
652
653
654
655
656
657
658
659
660
661
662
663
664
665
666
667
668
669
670
671
672
673

Observation		Confocal Technique		
		CRS	SCM	CCM
Magnification		× 50	× 10	× 10
Observable Area [μm^2]		40,000	722,823	722,823
Minimum Aggregate Size [μm^2]		3	11	3
Maximum Aggregate Size [μm^2]		1,589	7,172	11,046
	0.625 wt.%	12 ± 2	199 ± 18	150 ± 27
	1.250 wt.%	14 ± 2	215 ± 4	246 ± 39
No. of Aggregates	2.500 wt.%	25 ± 1	358 ± 96	337 ± 66
	5.000 wt.%	31 ± 7	436 ± 23	372 ± 46

674
675   Table 1
676
677
678
679
680
681
682
683
684
685
686
687
688
689
690
691
692
693
694
695
696
697
698
699
700
701

Technique	Category	Area Measurement	CNC content [wt.%]			
			0.625	1.25	2.5	5
SCM	Small	Median [μm²]	14[*]	17[*]	17[*]	22
		Range [μm²]	11-39[*]	11-44[*]	11-39[*]	11-80
	Medium	Median [μm²]	87[*]	105[*]	85[*]	160
		Range [μm²]	41-259[†*]	47-381[‡*]	41-287[*]	83-400
	Large	Median [μm²]	487[†*]	711	542[*]	823
		Range [μm²]	273-1,095[†*]	405-1,938[‡]	295-1,478[*]	416-2,735
CCM	Small	Median [μm²]	22[*]	25[*]	22[*]	36
		Range [μm²]	11-69[†*]	11-88[*]	11-88[*]	11-130
	Medium	Median [μm²]	150[‡*]	154[‡*]	207[*]	276
		Range [μm²]	72-386[‡*]	91-441[‡*]	91-612[*]	132-761
	Large	Median [μm²]	585[*]	758[‡*]	1260	1448
		Range [μm²]	405-1,823[‡*]	458-1,304[‡*]	662-3,739	772-5,733

702
703 Table 2
704